SENSITIVE VERY LONG BASELINE INTERFEROMETRY STUDIES OF THE OH MEGAMASER EMISSION FROM IRAS 17208−0014

E. MOMJIAN,[1] J. D. ROMNEY,[2] C. L. CARILLI,[2] AND T. H. TROLAND[3]

ABSTRACT

We present phase-referenced VLBI results on the radio continuum and the OH 18 cm megamaser emission from the ultraluminous infrared galaxy, IRAS 17208−0014. The observations were carried out at 1599 MHz using the Very Long Baseline Array, the phased VLA, and the Green Bank Telescope. The highest resolution radio continuum results show several compact sources with brightness temperatures on the order of 10^6 K. These sources are more likely to be clustered supernova remnants and/or luminous radio supernovae. However, the agreement between the number of observed and expected compact sources above the $5\,\sigma$ level supports the possibility that each one of the compact sources could be dominated by a recently detonated luminous radio supernova. The continuum results suggest that there are no radio-loud AGNs in the nuclear region of this galaxy. The OH 18 cm megamaser emission in IRAS 17208−0014 is detected at various angular resolutions. It has an extent of 170 pc × 110 pc and is mostly localized in two regions separated by 61 pc. The structure and dynamics of the maser emission seem to be consistent with a clumpy, rotating, ringlike geometry, with the two dominant maser regions marking the tangential points of the proposed rotating-ring distribution. Assuming Keplerian motion for the rotating maser ring, the enclosed dynamical mass and the mass density within a radius of 30.5 pc are about $3 \times 10^7 (\sin^{-2} i)\, M_\odot$ and $281 (\sin^{-2} i)\, M_\odot\ \mathrm{pc}^{-3}$, respectively.

Subject headings: galaxies: individual (IRAS 17208−0014) — galaxies: starburst — radio continuum: galaxies — radio lines: galaxies — techniques: interferometric

1. INTRODUCTION

At bolometric luminosities greater than $10^{11}\ L_\odot$, infrared galaxies become the most numerous objects in the local universe ($z \leq 0.3$; Sanders & Mirabel 1996). The trigger for the intense infrared emission appears to be the strong interaction or merger of molecular gas-rich spirals. Galaxies with the highest infrared luminosities [$L_{IR}(8$–$1000\ \mu m) \geq 10^{12}\ L_\odot$], known as ultraluminous infrared galaxies (ULIRGs), appear to be advanced merger systems powered by a nuclear starburst and/or an active galactic nucleus (AGN). These may represent an important stage in the formation of quasi-stellar objects (Sanders et al. 1988).

The extreme merging conditions in ULIRGs could, in some cases, induce nuclear OH 18 cm masing several orders of magnitude stronger than for typical Galactic masers, i.e., megamasers (10^6 times), or even gigamasers (10^9 times; Baan 1989; Baan et al. 1992). Recent surveys by Darling & Giovanelli (2002) report an OH megamaser (OHM) detection rate of up to 33% for ULIRGs at $z > 0.1$.

Sensitive Very Long Baseline Interferometry (VLBI) observations provide the most direct means to study OHMs and radio continuum emission in the innermost, dust-obscured regions of merging systems. While radio continuum studies play a key role in directly imaging and determining the nature of the nuclear power sources (AGNs and/or starbursts) in these galaxies, the OHM emission studies can enhance our understanding of the kinematics on parsec scales in their nuclear regions, and be used as probes of AGNs or intense nuclear starbursts.

In the present paper, we report VLBI observations of the 18 cm radio continuum and OHM emission from the galaxy IRAS 17208−0014 at $z = 0.04281$. This object is one of the few strong OHM emitters at $z < 0.1$ that can be imaged at milliarcsecond resolution and contribute to a better understanding of the nature, extent, and dynamics of extragalactic OHM emission.

This galaxy, which is classified as a ULIRG, has an infrared luminosity of $L_{IR} = 2.5 \times 10^{12}\ L_\odot$, as defined in Goldader et al. (1995). We adopt a distance of 171 Mpc, assuming $H_0 = 75\ \mathrm{km\ s^{-1}\ Mpc^{-1}}$. At this distance, 1 mas corresponds to 0.76 pc.

Optical images of IRAS 17208−0014 at 6550 Å show two tidal tails from a merger (Melnick & Mirabel 1990; Murphy et al. 1996). Near-IR images show a very disturbed morphology and an extended, but single, nucleus, suggesting a very advanced merger (Zenner & Lenzen 1993; Murphy et al. 1996). Infrared observations suggest that this galaxy represents the extreme of starburst-dominated sources of this type (Soifer et al. 2000), and an observational proof that a collision of galaxies can lead to a mass distribution similar to elliptical galaxies (Zenner & Lenzen 1993).

The radio continuum emission of this galaxy at milliarcsecond resolution was first detected by the VLBI observations of Momjian et al. (2003) at 21 cm. These observations revealed that the radio emission is dominated by an extreme nuclear starburst, with no indication of a compact high-brightness temperature source (i.e., a radio-loud AGN).

IRAS 17208−0014 exhibits OHM activity at 1665, 1667, and 1720 MHz (Martin et al. 1989). The strongest emission is in the 1667 MHz line, with a luminosity of $L_{OH} = 1054\ L_\odot$ (Martin et al. 1989). Very Large Array (VLA) and single-dish Nançay observations showed the existence of two separate velocity structures with similar widths for both the 1667 and 1665 MHz OH main lines (Martin et al. 1989). However, the 18 cm VLBI observations of Diamond et al. (1999) did not detect the 1665 MHz line

[1] National Astronomy and Ionosphere Center, Arecibo Observatory, HC 3 Box 53995, Arecibo, PR 00612; emomjian@naic.edu.
[2] National Radio Astronomy Observatory, P.O. Box O, Socorro, NM 87801; jromney@nrao.edu, ccarilli@nrao.edu.
[3] University of Kentucky, Department of Physics and Astronomy, Lexington, KY 40506; troland@pa.uky.edu.
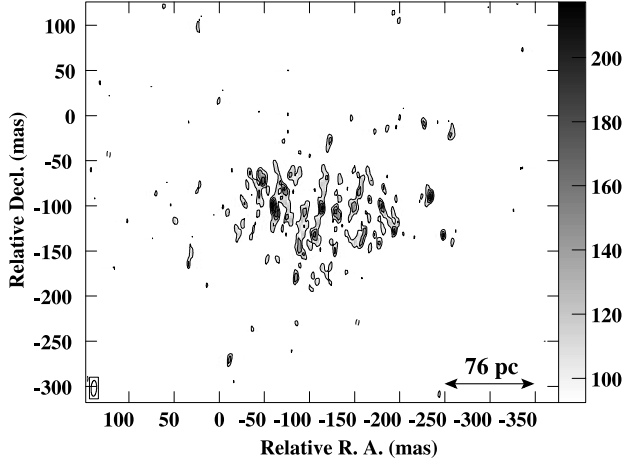
FIG. 1.—Continuum image of the central region in IRAS 17208−0014 at 1599 MHz. The restoring beam size is 17.6 mas × 6.1 mas at position angle −4°. The peak flux density is 217 μJy beam^{-1}, and the contour levels are at −3, 3, 4, 5, and 6 times the rms noise level, which is 31 μJy beam^{-1}. The gray-scale range is indicated by the wedge at the right side of the image. The reference position (0, 0) is α(J2000.0) = $17^h23^m21^s.9648$, δ(J2000.0) = −00°17′00″.819. For comparison purposes, this origin has been chosen to be the same as that in the continuum figures of Momjian et al. (2003).

or the continuum emission, and recovered only 20% of the 1667 MHz line.

2. OBSERVATIONS AND DATA REDUCTION

The present observations were carried out at 1599 MHz on 2003 May 25, using three NRAO[4] facilities: the Very Long Baseline Array (VLBA), the phased VLA, and the Green Bank Telescope. The bandwidth of the observations was 16 MHz in each of the right- and left-hand circular polarizations, with the central frequency set appropriately for the 1667 MHz transition of the OH 18 cm line at a heliocentric velocity $cz = 12,790$ km s^{-1} (Martin et al. 1989; Momjian et al. 2003). The data were two bit sampled and correlated at the VLBA correlator in Socorro, New

---

[4] The National Radio Astronomy Observatory is a facility of the National Science Foundation operated under cooperative agreement by Associated Universities, Inc.

Mexico, with 512 point spectral resolution per baseband channel and 2 s correlator integration time. The total observing time was 10 hr.

Data reduction and analysis were performed using the Astronomical Image Processing System (AIPS) and the Astronomical Information Processing System (AIPS++).

Along with the target source IRAS 17208−0014, the compact source J1730+0024 was observed as a phase reference. A cycle consisting of 180 s on the target source and 60 s on the reference source was adopted. The source J1743−0350 was used for amplitude and bandpass calibration.

After applying a priori flagging and manually excising integrations affected by interference, we performed amplitude calibration using the measurements of the antenna gain and system temperature of each station and bandpass calibration. The flux density calibration of the data set is believed to be accurate at the level of 5% (Wrobel & Ulvestad 2005).

A continuum data set was generated by averaging the OH emission−free spectral channels. In the continuum data set, the phase reference source J1730+0024, was self-calibrated and imaged in an iterative cycle. The self-calibration solutions for J1730+0024 were applied to both the continuum and line data of the target source.

The continuum and line data sets of IRAS 17208−0014 were then deconvolved and imaged at various spatial resolutions, with a grid weighting intermediate between pure natural and pure uniform (ROBUST = 0 in AIPS task IMAGR). The continuum images were obtained using the multiresolution CLEAN algorithm in IMAGR, which has been shown to be superior to the standard CLEAN or maximum entropy method in imaging a combination of very weak extended and compact emission regions (Momjian et al. 2003).

3. RESULTS

Figure 1 is the continuum image of the central region in IRAS 17208−0014 at 1599 MHz and 17.6 × 6.1 mas (13.4 × 4.6 pc, P.A. = −4°) resolution, and represents the bright emission region to the west of center in Figure 2 of Momjian et al. (2003). This region is populated by 10 compact sources with peak flux densities >5 σ (155 μJy beam^{-1}) but <7 σ (217 μJy beam^{-1}). Most of these sources were reproduced with pure natural weighting (ROBUST = 5), but not with pure uniform weighting (ROBUST = −5). This

TABLE 1
COMPACT SOURCES IN IRAS 17208−0014

| | | GAUSSIAN COMPONENT PARAMETERS | | | |
SOURCE (1)	RELATIVE POSITION[a] (mas) (2)	Peak[b] (μJy beam^{-1}) (3)	Total (μJy) (4)	Deconvolved Size[c] (pc) (5)	P.A. (deg) (6)
1................................	0, 0	177 ± 31	320 ± 81	9.3 × 5.0	5
2................................	13W, 32S	196 ± 30	604 ± 119	21.3 × 5.4	12
3................................	24W, 11S	164 ± 32	241 ± 71	9.8 × <7.1	...
4................................	57W, 60S	168 ± 31	299 ± 81	7.6 × 4.4	38
5................................	65W, 31S	185 ± 31	295 ± 75	10.7 × 3.0	10
6................................	81W, 36S	167 ± 31	307 ± 83	10.1 × <8.9	...
7................................	131W, 29S	166 ± 32	243 ± 71	12.3 × <2.3	...
8................................	146W, 55S	164 ± 32	210 ± 66	6.8 × 2.4	7
9................................	185W, 18S	184 ± 31	319 ± 79	7.1 × 5.4	177
10..............................	200W, 61S	167 ± 33	119 ± 45	<4.9	...

[a] The reference position (0, 0) is α(J2000.0) = $17^h23^m21^s.96158$, δ(J2000.0) = −00°17′00″.8904.
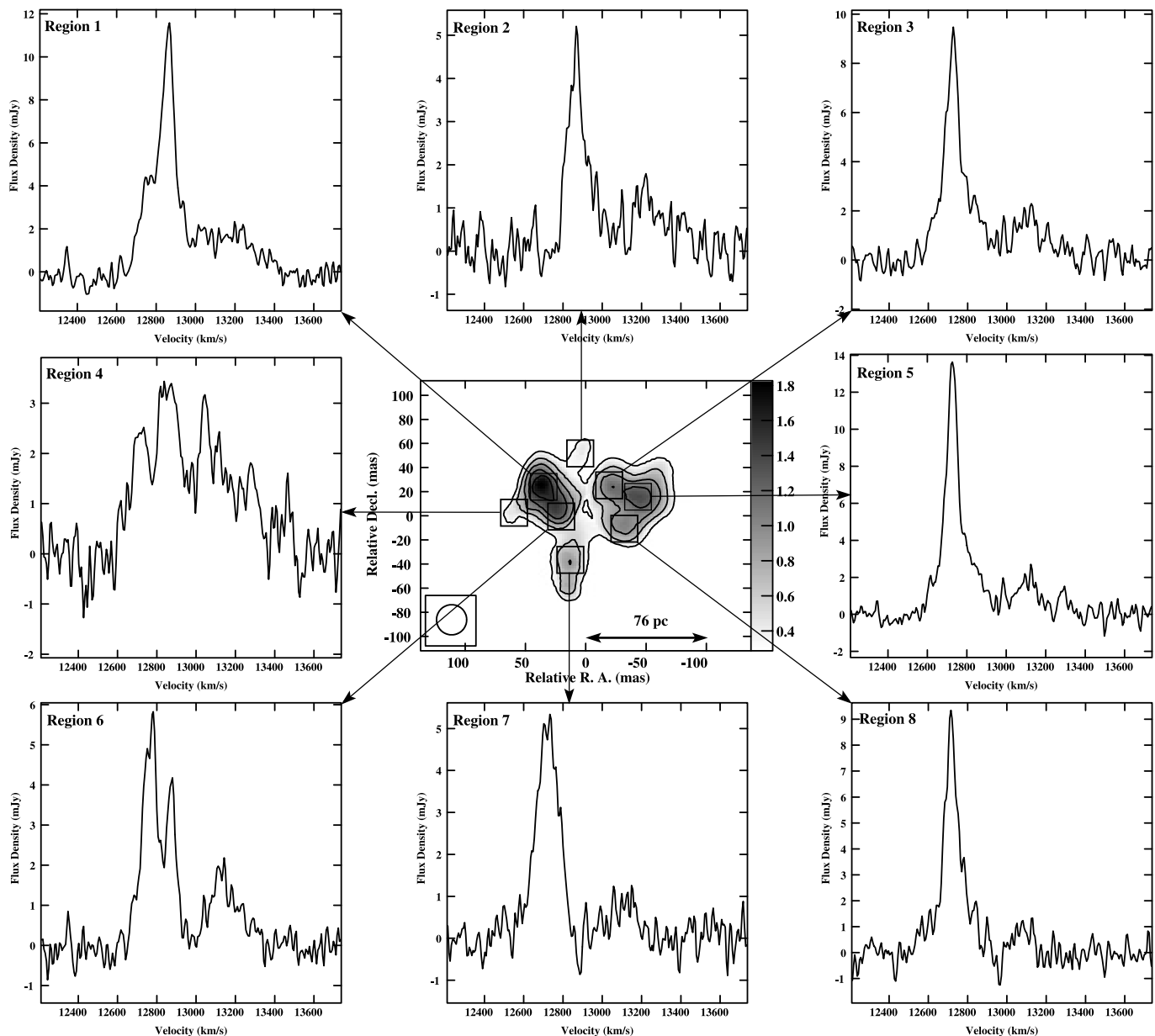[b] Higher than 5 σ = 155 μJy beam^{-1}.
[c] At half-maximum.

FIG. 2.—Gray-scale and contour total intensity (moment 0) image of the OH 18 cm main lines, and Hanning-smoothed OH spectra obtained at various locations of the OHM emission. The restoring beam size is 25 mas × 25 mas. The contour levels are at 0.3, 0.6, 0.9, 1.2, 1.5, and 1.8 Jy beam^{-1} km s^{-1}, and the gray-scale range is indicated by the step wedge at the right-hand side of the image in units of Jy beam^{-1} km s^{-1}. The reference position (0, 0) is α(J2000.0) = $17^h23^m21^s9533$, δ(J2000.0) = $-00°17'00''983$. The rms noise level of the total intensity is 0.13 Jy beam^{-1} km s^{-1}. The velocity scale of the spectra is referenced to the 1667 MHz line, and the spectral features between 13,000 and 13,400 km s^{-1} are from the 1665 MHz line (Martin et al. 1989). The effective velocity resolution of the spectra is 12.3 km s^{-1}.

is largely due to the much higher noise in the uniformly weighted image, which is a factor of 6 worse than natural weighting, and almost a factor of 4 worse than the intermediate weighting (ROBUST = 0). Table 1 lists the Gaussian fitting parameters of the compact continuum sources seen in Figure 1 derived using the AIPS task JMFIT. The positions (col. [2]) are relative to the first source in the list. Column (3) lists the surface brightnesses of these sources, and column (4) their integrated flux densities. Column (5) gives the deconvolved sizes of the Gaussian components at FWHM, and column (6) gives the position angles. For several of these components, the nominal deconvolution sizes are listed as given by JMFIT. However, for some components, no nominal sizes were obtainable for the minor axes of the fitted Gaussians, hence, the maximum sizes of the minor

axes are reported as upper limits. Moreover, because source 10 is unresolved, we are only able to quote an upper limit for its overall size. The corresponding brightness temperatures of these compact sources are on the order of 10^6 K.

Figure 2 is a total intensity (moment 0) image of the OH 18 cm main lines (both 1665 and 1667 MHz) at 25 mas resolution. The image was obtained by blanking areas where the flux density of the OH spectral-line image cube is below 4 σ, or 3.6 mJy beam^{-1}. Figure 2 also shows the Hanning-smoothed spectra of the OH 18 cm main lines averaged over various regions of the OHM emission.

OH emission from IRAS 17208−0014 is spread over a broad range of velocities. The strong, narrow feature seen in all profiles of Figure 2 (other than for region 4) almost certainly arises from

TABLE 2

Gaussian Parameters of the OH Megamaser Lines in the Regions of Figure 2

	1667 MHz			1665 MHz			
Region (1)	Velocity (km s^{-1}) (2)	ΔV_{FWHM} (km s^{-1}) (3)	F_{1667} (mJy beam^{-1}) (4)	Velocity (km s^{-1}) (5)	ΔV_{FWHM} (km s^{-1}) (6)	F_{1665} (mJy beam^{-1}) (7)	F_{1667}/F_{1665} (8)
1..........................	12864 ± 2	73 ± 4	12.3 ± 0.5	13193 ± 18	234 ± 40	2.0 ± 0.2	6.2 ± 0.5
2..........................	12861 ± 8	97 ± 13	4.8 ± 0.4	13217 ± 17	261 ± 44	1.3 ± 0.2	3.7 ± 0.5
3..........................	12727 ± 2	85 ± 4	11.3 ± 0.3	13095 ± 13	270 ± 34	1.9 ± 0.2	6.0 ± 0.4
5..........................	12727 ± 2	77 ± 4	13.4 ± 0.5	13103 ± 15	263 ± 39	1.6 ± 0.2	8.4 ± 0.5
6..........................	12768 ± 2	95 ± 5	8.0 ± 0.3	13140 ± 8	198 ± 18	2.2 ± 0.2	3.6 ± 0.4
	12875 ± 2	56 ± 4	6.1 ± 0.4	$\dots$	$\dots$	$\dots$	$\dots$
7..........................	12724 ± 2	128 ± 5	6.5 ± 0.2	13114 ± 11	139 ± 27	1.2 ± 0.2	5.4 ± 0.3
8..........................	12715 ± 3	82 ± 5	9.9 ± 0.4	13083 ± 10	95 ± 24	1.2 ± 0.3	8.3 ± 0.5

the 1667 MHz transition. This conclusion seems very likely for two reasons. First, this relatively narrow feature lies close to the systemic velocity of the galaxy if the feature arises from the 1667 MHz transition (see § 2). Second, this narrow feature is always accompanied by a weaker emission feature offset by about 370 km s^{-1}, the velocity equivalent to the difference in frequency between the 1665 and 1667 MHz lines at the redshift of IRAS 17208−0014.

The overall extent of the megamaser emission is 170 pc × 110 pc on the plane of the sky, and seems to be dominated by two regions separated by 80 mas (61 pc) at position angle 83°. We designate these the eastern and western components (regions 1 and 5 in Fig. 2). These two regions seem to be connected by weaker maser emission regions, interrupted in the middle by what seems to be a region devoid of maser emission. In addition to the two main maser regions, a weak extension toward the south, and an even weaker one toward the north are detected. The measured velocity difference between the eastern and the western regions is 137 ± 3 km s^{-1}.

Table 2 summarizes the physical characteristics of the dominant OH peaks seen in the spectra of Figure 2 for both the 1665 and the 1667 MHz transitions. The line properties were obtained by fitting Gaussians to the non−Hanning-smoothed OH spectra obtained in the regions specified in Figure 2, using the tool IMAGEPROFILEFITTER in AIPS++. Column (1) lists the region number, as designated in Figure 2. The velocities (col. [2]) refer to the center velocities of the 1667 MHz line peaks in each region. Column (3) lists their full widths at half maximum, and column (4) is their peak flux density values. Columns (5)–(7) are similar to columns (2)–(4), but for the 1665 MHz line peaks. Column (8) is the peak flux density ratio of the 1667 MHz line to the 1665 MHz line for each region. For the spectrum of region 6, which shows two distinct emission peaks for the 1667 MHz line, two Gaussian components are listed. No Gaussian fitting parameters are reported for the spectrum seen in region 4 because of its low signal-to-noise ratio and the apparent blending of the two mainlines.

Figure 3 is a Hanning-smoothed spectrum of the OH 18 cm main lines integrated over the whole OH emission region seen in Figure 2. The velocity scale is referenced to the 1667 MHz line. The weak emission between 13,000 and 13,400 km s^{-1} is from the 1665 MHz main line (Martin et al. 1989). The arrow in this figure points to the expected velocity of the 1665 MHz line that corresponds to the main peak of the 1667 MHz line. While the shape of the spectral profile seen in Figure 3 is similar to that obtained at Nançay and with the VLA (Martin et al. 1989), the

VLBI array recovers only ∼80% of the single-dish and VLA flux densities.

Figure 4 displays gray-scale total intensity (moment 0) images of the 1667 MHz main line at three different angular resolutions with continuum contours superposed. For comparison purposes, the same origin is used for the coordinates as by Momjian et al. (2003) for their continuum images. Figure 4a is at 50 mas resolution, Figure 4b at 25 mas resolution, and Figure 4c at the full resolution of the VLBI array, which is 17.6 mas × 6.1 mas resolution (P.A. = −4°). These images were obtained by restricting the spectral channel range to that of the 1667 MHz main line, and blanking the OH image cubes at the 4 σ level, where σ is 1.8, 0.9, and 0.5 mJy beam^{-1}, for the 50 and 25 mas and the full-resolution images, respectively. In all these images, the OH emission from the eastern region appears to be stronger than that from the west. The lower resolution images show the eastern region to be associated with stronger continuum emission than the western
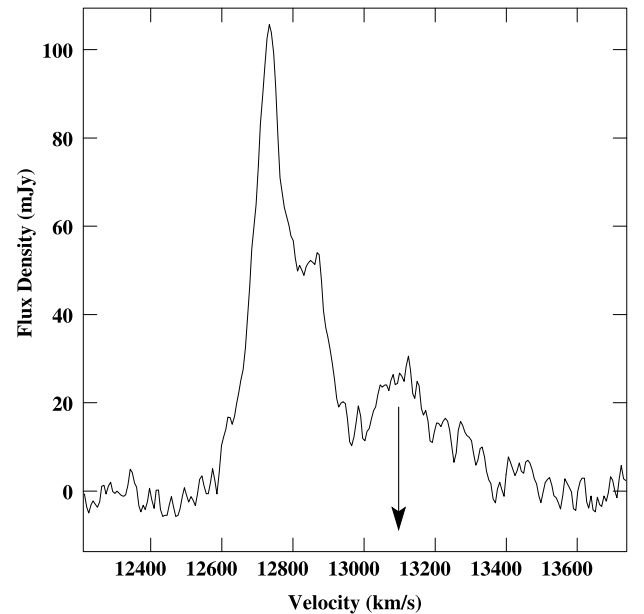

Fig. 3.—Hanning-smoothed OH 18 cm spectrum integrated over the complete OH emission region as seen in our VLBI observations. The velocity scale is referenced to the 1667 MHz line. The effective velocity resolution is 12.3 km s^{-1}. The arrow points to the expected velocity of the 1665 MHz line that corresponds to the main peak of the 1667 MHz line. At the redshift of IRAS 17208−0014, the offset between these two lines is 368 km s^{-1}.
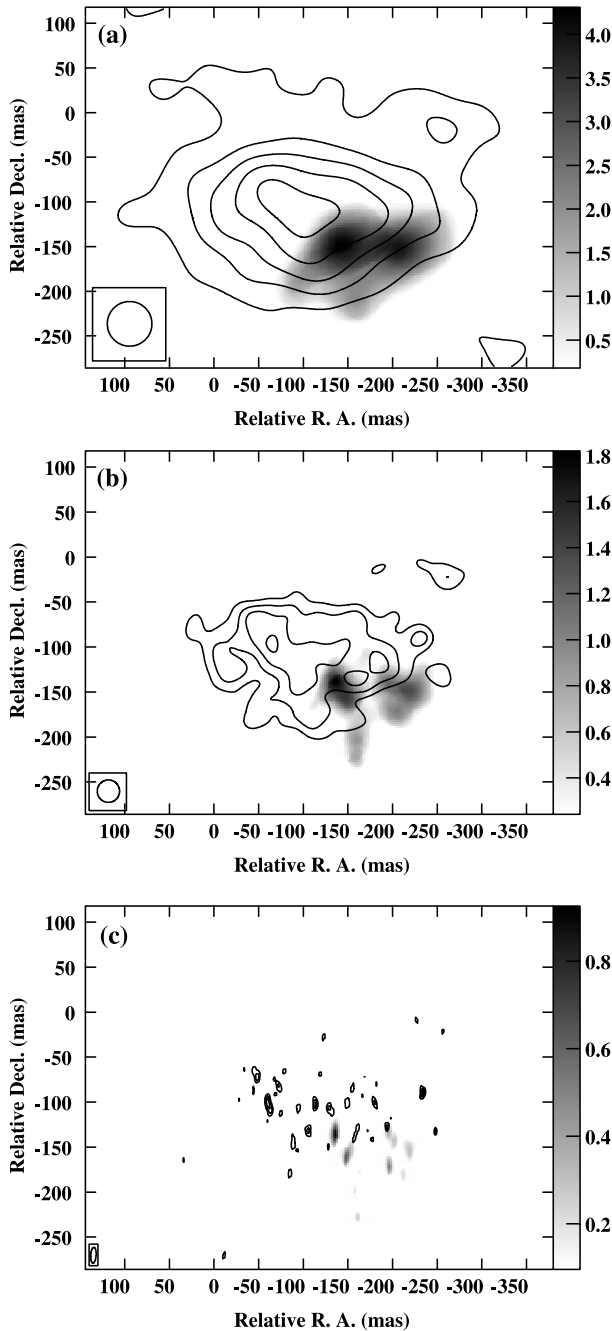
Fig. 4.—Gray-scale total intensity (moment 0) images of the 1667 MHz OH 18 cm main line, with 1599 MHz continuum contours superposed, at various angular resolutions. (a) 50 mas resolution. Contour levels are at 4, 8, 12, 16, and $20 \times 1~\sigma$ (89 μJy beam^{-1}). (b) 25 mas resolution. Contour levels are at 4, 6, 8, and $10 \times 1~\sigma$ (57 μJy beam^{-1}). (c) Full resolution of the array (17.6 mas $\times$ 6.1 mas, P.A. $= -4°$). Contour levels are at 4, 5, and $6 \times 1~\sigma$ (31 μJy beam^{-1}). The reference position (0, 0) is the same as in Fig. 1. The gray-scale range in all these images is indicated by the step wedge at the right-hand side of each image in units of Jy beam^{-1} km s^{-1}.

Fig. 5.—OH 1667 MHz velocity field (moment 1) at 50 mas resolution. Contours are from 12,700 to 12,850 km s^{-1} in steps of 25 km s^{-1}. The gray-scale range is between 12,670 and 12,910 km s^{-1}. The reference position (0, 0) is the same as in Fig. 2.

be distorted toward the western region. Moreover, the eastern region itself shows a north-south velocity gradient.

4. DISCUSSION

4.1. *The Radio Continuum*

The radio continuum emission from the ULIRG IRAS 17208−0014 at 1362 MHz has been discussed in detail by Momjian et al. (2003) for various angular resolutions. Our observations at 1599 MHz have imaged the radio continuum emission from IRAS 17208−0014 at a considerably higher angular resolution than previously reported, which was 36 mas $\times$ 33 mas, P.A. 25° (Momjian et al. 2003).

The continuum image at the full resolution of our VLBI array (i.e., 17.6 mas $\times$ 6.1 mas; Fig. 1) shows several compact sources with flux densities greater than 5 times the rms noise level of 155 μJy beam^{-1}. We find no dominant compact radio source with a very high brightness temperature. The brightness temperatures of these sources are on the order of 10^6 K, indicating that the emission is nonthermal.

Following the discussion in Momjian et al. (2003) and references therein, these compact sources are likely to be clustered radio supernovae (RSNe) and/or supernova remnants (SNRs), with a likelihood that each of these sources could be mainly powered by a recently detonated individual RSN. Using the post-maximum light curve of luminous RSNe derived by Smith et al. (1998), we find that individual RSNe will lie above our 5 σ detection level for 3.6 yr. Given the supernova rate of 4 ± 1 yr^{-1} in IRAS 17208−0014 (Momjian et al. 2003), we expect to see about 14 ± 4 individual RSNe. This is in good agreement with the 10 sources revealed in our observations.

We defer further discussion of the continuum emission to a subsequent paper, in which we hope to report lower angular resolution results at 1599 MHz with matching-resolution lower frequency VLBI continuum observations at 330 and 610 MHz, and higher frequency MERLIN continuum observations at 5 GHz.

4.2. *The OHM Emission*

The spectral-line observations reported here reveal the details of the OHM emission from IRAS 17208−0014. The maser emission is complex, and seems to be localized in two distinct areas, the eastern and western components, separated by 61 pc (Fig. 2).

region. Moreover, the continuum emission seems to have a larger extent than that of the OHM, and its peak is located northeast of the megamaser regions. At full resolution, we find no correlation between the brightest continuum and maser emission spots. The derived lower limit on the maser amplification factor is ∼130.

Figure 5 is the velocity field (moment 1) of the 1667 MHz main line at 50 mas resolution. A general velocity gradient is seen in the east-west direction; however, the velocity contours seem to
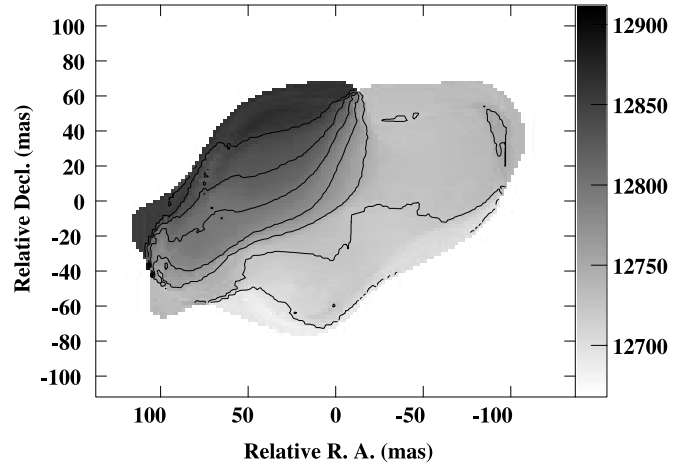
Weaker maser emitting regions can be seen toward the north and the south.

Our VLBI observations recover ∼80% of the single-dish flux density of the OHM emission in IRAS 17208−0014 (Martin et al. 1989). This suggests that extended OH emission is resolved by even the shortest baseline in our VLBI array, namely the phased-VLA to Pie Town baseline (52 km), and indicates that such emission regions have angular extents of at least 0″.37. This is well within the ∼5″ extent of the galaxy as seen in multiwavelength IR observations (Soifer et al. 2000).

The overall nature, geometrical distribution, and kinematics of the megamaser emission in IRAS 17208−0014 show striking similarities to those of another megamaser galaxy, III Zw 35; see Pihlström et al. 2001 and Parra et al. 2005. These authors explain the OH emission in III Zw 35 by invoking the presence of an inclined clumpy ring structure oriented in a north-south direction. A similar ring model, although with an east-west orientation, could describe the OH emission in IRAS 17208−0014. In such a model, the two strongest emission peaks, the eastern and western components (Fig. 2), would mark directions tangential to the ring, and the apparent empty region in the middle would coincide with the center of the ring. Assuming a circular ring structure, and excluding the southern and northern regions seen in Figure 2, the apparent extent of the OHM emission on the plane of the sky suggests an inclination angle of ∼55°. Numerical simulations and modeling, however, are needed to derive a more reliable estimate for the inclination angle.

In addition to the eastern and western components, the OHM emission in IRAS 17208−0014 shows a prominent extension to the south at various angular resolutions. This structure does not seem to be part of the proposed ring structure, but lies perpendicular to it. Considering its position, width, and velocity (Fig. 2 [region 7] and Table 2), this feature could be associated with an inflow or an outflow. Molecular outflows and inflows have been previously reported in several megamaser galaxies, sometimes with velocities up to 800 km s^{-1} (Baan et al. 1989; Pihlström et al. 2005). Simulations carried out by Mihos & Hernquist (1996) show that when gas-rich galaxies merge, strong gravitational torques drive the gas to the center of the remnant as a strong inflow and fuel an intense but very short-lived starburst. Considering that IRAS 17208−0014 is an advanced merger system powered by an extreme starburst (Zenner & Lenzen 1993; Murphy et al. 1996; Momjian et al. 2003), the southern extension could be the result of an inflow that is fueling the starburst. Alternatively, the southern extension could be associated with an outflow. Extreme merging conditions, and consequently powerful nuclear activity (AGN and/or starburst), could induce superwinds in the nuclear region and cause material to be blown away. However, our data cannot uniquely establish whether the southern extension is an inflow or an outflow. Considering that another, weaker, extension is seen to the north (region 2 of Fig. 2), it might be the case that both the northern and southern extensions are part of another rotating structure, or they may represent different maser spots in a turbulent velocity field.

The larger extent of the continuum emission relative to that of the OHM emission in IRAS 17208−0014 (Figs. 4a and 4b) indicates that the star formation in the nuclear region of this galaxy is not confined to just around or within the proposed ring structure, suggesting that the OH population inversion occurs only over a small region. This is likely because the inversion of the OH main lines depends critically on the local IR spectrum (see Parra et al. 2005 and references therein). Moreover, these two images show that the OHM and peak continuum intensities do not coincide. This can be explained by free-free absorption, as

was suggested for III Zw 35 (Pihlström et al. 2001). If the optical depth is significant at 1.6 GHz ($\tau > 1$), then the emission measure EM $= n_e^2 l > 6 \times 10^6$ pc cm^{-6}. Assuming $l \sim 100$ mas (76 pc), then the density is $n_e > 281$ cm^{-3}, which is consistent with that expected for a dense starburst nucleus (Sanders & Mirabel 1996). Our subsequent paper on multifrequency VLBA and MERLIN continuum observations will address the likelihood of free-free absorption in IRAS 17208−0014. Another possibility is that this system is an incomplete merger, in which the nuclei of the progenitor galaxies have not yet completely merged. The OH ring traces one of the original nuclei, and the star formation in the center is asymmetrically distributed around this nucleus.

At the full resolution of the array, the lack of positional coincidence between the continuum and megamaser spots in IRAS 17208−0014 (Fig. 4c) is also found in other OHM galaxies, e.g., Arp 220, III Zw 35, and Mrk 273 (Lonsdale et al. 1998; Pihlström et al. 2001; Klöckner & Baan 2004). The derived lower limits on the maser amplification factors in IRAS 17208−0014 are up to 130. Lonsdale et al. (1998) and Diamond et al. (1999) estimate that the amplification factors of the megamaser emission in Arp 220 and III Zw 35 are up to 800 and 500, respectively. Furthermore, these authors explain the lack of positional correlation between the continuum and the OHM spots by saturated compact masing clouds. However, Parra et al. (2005), based on their detailed modeling of the OHM emission in III Zw 35, propose instead that the masers could be unsaturated. The brightest maser emission could occur in regions where the continuum emission is either very weak or below the current detection threshold, because of the exponential effect of path length on unsaturated masers occurring in clumpy media (Parra et al. 2005).

The measured 1667−1665 MHz flux density ratio at various regions of the OHM emission varies between 3.6 ± 0.4 and 8.4 ± 0.5 (Table 2). Similar high 1667−1665 MHz ratios are reported in other OHM galaxies, such as Mrk 273 and III Zw 35 (Yates et al. 2000; Pihlström et al. 2001). These high ratios clearly indicate that the OH molecular levels are not in local thermodynamic equilibrium (LTE), which would yield a ratio of 1.8 (Henkel & Wilson 1990). Moreover, the line ratios of the eastern and western OHM regions (regions 1 and 5, Fig. 2 and Table 2) in IRAS 17208−0014, which are the tangents of the proposed ring structure, are very similar to those of the tangent points in III Zw 35 (Pihlström et al. 2001). Based on the very high 1667−1665 MHz line ratios observed in Arp 220, Lonsdale et al. (1998) have suggested the existence of two maser emission phases. One is compact, characterized by saturated high-gain masers, and the other diffuse, characterized by unsaturated low-gain masers. However, Pihlström et al. (2001) have proposed instead a mechanism for OHM emission based on a single phase of OH masing small clouds (∼1 pc), and Parra et al. (2005) have argued that the observed differences in the line ratios between compact and diffuse phases could be a natural property of one phase characterized by clumpy unsaturated masers, in agreement with the classical megamaser model of Baan (1989). Furthermore, our results suggest that higher line ratios seem to be correlated with slightly narrower 1667 MHz line widths. Regions with line ratios greater than 6 show velocity widths between 73 and 85 km s^{-1}, while regions with lower line ratios display velocity widths between 95 and 128 km s^{-1}. Therefore, higher 1667−1665 MHz line ratios can be explained by the exponential amplification of the background radiation by overlapping unsaturated maser clouds in both space and velocity (Parra et al. 2005; Lockett & Elitzur 2005).

The exponential amplification that causes stronger 1667 MHz lines, and consequently higher 1667−1665 MHz line ratios, could also explain the narrower measured widths of the 1667 MHz lines

compared to those at 1665 MHz (Table 2). While the 1667 MHz transition exhibits a range of strong and weak features in a given region (Fig. 2), the 1665 MHz counterparts will have a smaller range of amplitudes, and appear as a wider, blended spectral feature.

The similarities between the OHM emission in IRAS 17208−0014 and III Zw 35, and consequently the proposed ring model, are further supported by the observed velocity field in IRAS 17208−0014 (Fig. 5). This field shows a strong gradient in the eastern region in two perpendicular directions, east-west and north-south, and a distorted field in the western region. A similar velocity field has been observed in III Zw 35 (Pihlström et al. 2001), where the northern masing region has a two-directional velocity gradient, and the southern region has a distorted velocity field.

To explain the observed velocity field with the ring model for the OHM emission in III Zw 35, Parra et al. (2005) have proposed that masing clouds, in addition to their rotational velocity, have a comparable outflow velocity parallel to the ring axis and directed away from the ring midplane. In the terminology of these authors, a cloud near a tangent region that lies above the ring midplane will have a projected outflow velocity that is blueshifted, while a cloud below the ring midplane will have a redshifted projected outflow velocity. Such a mechanism could produce an apparent velocity difference of nearly twice the projected outflow velocity, and would be perpendicular to the rotational velocity of the ring. These authors further note that at the tangent point where material is moving away from the observer, i.e., the northern tangent point in III Zw 35, or the eastern tangent point in IRAS 17208−0014, the cloud outflow mechanism gives a velocity gradient in the same direction as that caused by the rotation mechanism, thus reinforcing the gradient. In contrast, the tangent point where material is moving toward the observer, i.e., the southern tangent point in III Zw 35, or the western tangent point in IRAS 17208−0014, the two mechanisms have opposite directions and will partly cancel. This could result in the distorted velocity field seen in the southern component of III Zw 35, or in the western component of IRAS 17208−0014. However, Parra et al. (2005) have suggested that, alternatively, the difference may mainly be due to the statistical nature of the clumpy maser model used in their Monte Carlo simulations.

While various regions of the OHM emission show one dominant spectral peak in the 1667 MHz line, region 6 (Fig. 2 and Table 2) displays a double spectral feature, suggesting the existence of a velocity substructure in this region. Considering that bright OHM emission spots are the result of spatial and velocity alignment of a number of unsaturated maser clouds (Parra et al. 2005), the observed double-peak spectrum indicates that there are two distinct aligned groups of masing clouds within this region.

Assuming a rotational velocity of $\sim$69 $\sin i$ km s^{-1}, the velocity gradient between the eastern and western masing peaks in IRAS 17208−0014, i.e., the tangents of the proposed ring distribution, is $\sim$2.3 $\sin i$ km s^{-1} pc^{-1}. For a radius of 30.5 pc, we derive an enclosed dynamical mass of about $3 \times 10^7 (\sin^{-2} i)$ $M_\odot$. A greater mass value is estimated on larger scales from molecular (CO) and atomic (H I) gas (Downes & Solomon 1998; Momjian et al. 2003). Within a radius of 30.5 pc, the measured mass density from the OH observations is 281($\sin^{-2} i$) $M_\odot$ pc^{-3}.

The large-scale velocity field attributed to the rotating ring structure is comparable to or smaller than the 1667 MHz line widths obtained at various regions of the ring (Table 2). Very similar rotational velocity and velocity widths are reported in III Zw 35 (Pihlström et al. 2001; Parra et al. 2005). These velocity widths, although very wide compared to galactic OH masers, seem to be typical for OHM sources. In their VLBI study of Arp 220,

Lonsdale et al. (1998) suggest that much of the broad megamaser line width is intrinsic to the compact maser spots. Moreover, Parra et al. (2005) explain that the observed line widths cannot arise from a population of narrow-width clouds, but from the spectral blending of masing clouds with internal velocity widths $\gg$1 km s^{-1}. In their detailed modeling of the OHM emission from III Zw 35, these authors report that in order to fit the observed velocity width of the compact maser spots, their model required maser clouds with internal velocity dispersion of 20 km s^{-1}. The high velocity dispersion of the OHM clouds indicates a highly turbulent medium, and suggests that the clouds are not gravitationally confined (Parra et al. 2005).

5. CONCLUSIONS

We have presented the results of sensitive, phase-referenced VLBI observations of the 18 cm continuum and OH megamaser emission in the central 0.4 kpc of the ULIRG IRAS 17208−0014.

The continuum emission from this galaxy was imaged at a higher resolution than has been previously reported. Several compact sources with flux densities greater than 5 σ were detected. These sources have brightness temperatures on the order of 10^6 K, and are more likely to be clustered RSNe and SNRs. However, we cannot rule out the possibility that each of the compact sources is mainly powered by an individual bright RSN nested in a region that contains faded SNRs. This is supported by the agreement in the number of the observed and expected continuum sources above the 5 σ level. The continuum results do not reveal a radio-loud AGN in the nuclear region of this galaxy.

The OHM results show the detection of both the 1665 and 1667 MHz mainlines in IRAS 17208−0014. The OHM emission in this ULIRG has an extent of 170 pc $\times$ 110 pc, and is mostly localized in two regions separated by 80 mas (61 pc). The overall structure and dynamics of the maser emission seem to be consistent with a clumpy, rotating, ringlike geometry, with the two dominant maser regions marking the tangential points of the proposed ring structure. However, our OH results reveal another component extending to the south. Considering the ongoing intense starburst in this advanced merger system, the southern extension could to be associated with a gaseous inflow or outflow. Assuming Keplerian motion for the observed OH ring structure, the enclosed dynamical mass and the mass density within a radius of 30.5 pc, are about $3 \times 10^7 (\sin^{-2} i)$ $M_\odot$ and 281($\sin^{-2} i$) $M_\odot$ pc^{-3}, respectively.

Our results show that the starburst activity, as seen in the radio continuum images, has a larger extent than the OHM emission. Moreover, the low-resolution images show that at larger scales the OHM emission peaks do not coincide with the peak of the continuum emission. This could be the result of free-free absorption and/or possibly an indication that the merger is incomplete. At the full angular resolution, the brightest continuum and OHM spots are not correlated. The derived lower limits on the maser amplification are up to 130.

The observed line-to-continuum ratios, 1667−1665 MHz line ratios, and the 1667 MHz line widths suggest that the strong OHM emission in various regions can be explained by unsaturated masing clouds overlapping in both space and velocity.

REFERENCES

Baan, W. A. 1989, ApJ, 338, 804

Baan, W. A., Haschick, A. D., & Henkel, C. 1989, ApJ, 346, 680

Baan, W. A., Rhoads, J., Fisher, K., Altschuler, D. R., & Haschik, A. 1992, ApJ, 396, L99

Darling, J., & Giovanelli, R. 2002, AJ, 124, 100

Diamond, P. J., Lonsdale, C. J., Lonsdale, C. J., & Smith, H. E. 1999, ApJ, 511, 178

Downes, D., & Solomon, P. M. 1998, ApJ, 507, 615

Goldader, J. D., Joseph, R. D., Doyon, R., & Sanders, D. B. 1995, ApJ, 444, 97

Henkel, C., & Wilson, T. L. 1990, A&A, 229, 431

Klöckner, H.-R., & Baan, W. A. 2004, A&A, 419, 887

Lockett, P., & Elitzur, M. 2005, BAAS, 37, 1191

Lonsdale, C. J., Diamond, P. J., Smith, H. E., & Lonsdale, C. J. 1998, ApJ, 494, L239

Martin, J. M., Bottinelli, L., Dennefeld, M., Gouguenheim, L., & Le Squeren, A. M. 1989, A&A, 208, 39

Melnick, J., & Mirabel, I. F. 1990, A&A, 231, L19

Mihos, J. C., & Hernquist, L. 1996, ApJ, 464, 641

Momjian, E., Romney, J. D., Carilli, C. L., Troland, T. H., & Taylor, G. B. 2003, ApJ, 587, 160

Murphy, T. W., Jr., Armus, L., Matthews, K., Soifer, B. T., Mazzarella, J. M., Shupe, D. L., Strauss, M. A., & Neugebauer, G. 1996, AJ, 111, 1025

Parra, R., Conway, J. E., Elitzur, E., & Pihlström, Y. M. 2005, A&A, 443, 383

Pihlström, Y. M., Baan, W. A., Darling, J., & Klöckner, H.-R. 2005, ApJ, 618, 705

Pihlström, Y. M., Conway, J. E., Booth, R. S., Diamond, P. J., & Polatidis, A. G. 2001, A&A, 377, 413

Sanders, D. B., & Mirabel, I. F. 1996, ARA&A, 34, 749

Sanders, D. B., Soifer, B. T., Elias, J. H., Madore, B. F., Matthews, K., Neugebauer, G., & Scoville, N. Z. 1988, ApJ, 325, 74

Smith, H. E., Lonsdale, C. J., Lonsdale, C. J., & Diamond, P. J. 1998, ApJ, 493, L17

Soifer, B. T., et al. 2000, AJ, 119, 509

Wrobel, J. M., & Ulvestad, J. S. 2005, Very Long Baseline Array Observational Status Summary (Soccorro: NRAO), http://www.vlba.nrao.edu/astro/obstatus/current

Yates, J. A., Richards, A. M. S., Wright, M. M., Collett, J. L., Gray, M. D., Field, D., & Cohen, R. J. 2000, MNRAS, 317, 28

Zenner, S., & Lenzen, R. 1993, A&AS, 101, 363